Device modeling for split-off band detectors

S. G. Matsik,[1] P. V. V. Jayaweera,[1] A. G. U. Perera,[1,a)] K. K. Choi,[2] and P. Wijewarnasuriya[2]
[1]*Department of Physics and Astronomy, Georgia State University, Atlanta, Georgia 30303, USA*
[2]*U.S. Army Research Laboratory, Adelphi, Maryland 20783-1197, USA*

(Received 30 April 2009; accepted 12 August 2009; published online 18 September 2009)

An approach to develop room temperature detectors is to use transitions between the light/heavy hole bands and the split-off hole band to produce enhanced response at high temperature. Results are presented on a theoretical model to predict the response in these split-off detectors. The model calculates the dark and illuminated currents from the photoabsorption, carrier escape, and transport, explaining the experimental response. The variation in dark current, responsivity, and D^* with the detector parameters is presented. © *2009 American Institute of Physics*. [doi:10.1063/1.3224873]

I. INTRODUCTION

Infrared detectors operating at high temperatures are of great importance for practical applications in the IR range. The use of room temperature or thermoelectrically cooled detectors would greatly reduce the weight and/or power requirements enhancing their attraction in practical applications. In addition to the InSb and PbSe detectors for the 3–5 μm range are HgCdTe operating up to 200 K,[1] quantum well,[2] quantum dot,[3] and type-II strained superlattice[4] detectors are being studied. The split-off band detectors offer a new approach to the IR detection with the capability of high operating temperatures.

The split-off band detection was initially observed for the 2–3 μm range in heterojunction interfacial workfunction internal photoemission (HEIWIP) detectors[5] and was confirmed using detectors specifically designed for the split-off detection mechanism,[6] which showed response up to 330 K. These detectors consist of multiple periods of highly doped emitter and undoped barrier layers between two highly doped contacts. The detection mechanism uses an absorption involving a transition from the light/heavy hole bands into the split-off hole band of the emitters. The photoexcited carriers must then escape over the band offset at the interface either directly in the split-off band or by scattering into the light/heavy hole bands. The escaped carriers are then swept out of the active region by an external electric field and collected at the contacts. Initial studies indicate that these detectors are capable of covering a wide wavelength range from the near infrared (NIR) to terahertz with the ability to design detectors for room temperature or thermoelectric (TE) cooled operation. Until now there has not been a complete model for the performance of the split-off detectors. In this paper, such a model is presented, the calculated results are compared with the experimental results, and potential improvements to the design are suggested.

II. BASIC MODELING FOR SPLIT-OFF BAND DETECTORS

The split-off band detector response model consists of five parts: (i) calculation of absorption in the emitters, (ii) calculation of excited carrier transport to the emitter/barrier interface, (iii) calculation of escape probability at the emitter/barrier interface, (iv) calculation of capture rate for injected carriers in the emitters, and (v) calculation of the dark and photocurrents.

As a preliminary to these calculations, the energy bands are determined in the emitter layer for use in determining the absorption and scattering rates for the various mechanisms. The bands were calculated using an eight band $\boldsymbol{k}\cdot\boldsymbol{p}$ approach[7] with the basis vectors and the Hamiltonian defined following the notation in Scholz.[8] The band structure was calculated once and then stored for use in the absorption and scattering calculations. Although the emitters in the test structure were GaAs, this approach can be readily extended to other materials by changing the input parameters to the band model which mostly consists of the observed band gaps and carrier masses.

A. Absorption modeling

The IR absorption in the emitter layer consists of two components, a direct absorption involving only the photon and the hole and an indirect absorption involving an additional scattering to conserve momentum. The two processes were calculated separately and then combined to give the total absorption.

1. Direct absorption transitions

The direct absorption will be from the light or heavy hole bands to the split-off band. The absorption in a unit cell of volume V for the direct transition is given by[9]

$$R = \frac{2V}{(2\pi)^3}\int d^3k(2\pi/\hbar)|\langle nk|H_{\rm int}|n'k'\rangle|^2 f(n,k) \times[1-f(n',k')]\delta(E'-E-\hbar\omega), \quad (1)$$

where $H_{\rm int}$ is the interaction of the photons with the carriers, n and n' indicate the initial and final bands, and $f(n,k)$ is the occupation of the $n^{\rm th}$ band at wavenumber k. Since the photon momentum should be negligible, momentum conservation will give $k'=k$. The matrix elements for $H_{\rm int}$ are given by

a)Electronic mail: uperera@gsu.edu.

 © 2009 American Institute of Physics

Downloaded 11 Jan 2010 to 131.96.4.68. Redistribution subject to AIP license or copyright; see http://jap.aip.org/jap/copyright.jsp

$$\langle nk|H_{\rm int}|n'k'\rangle = -(eA_0/2m)(\mathbf{a}\cdot\mathbf{p}). \qquad (2)$$

2. Indirect absorption transitions

The indirect transition will involve a third particle (either a phonon or an impurity) to conserve momentum and is calculated using second order perturbation theory. The absorption in a unit cell is given by

$$R = \frac{2V^2}{(2\pi)^6}\int d^3k d^3k' S f(k)[1-f(k')], \qquad (3)$$

where

$$S = \frac{2\pi}{\hbar}|\langle n'k'|H_{\rm scat}|nk\rangle|^2|\langle n''k''|H_{\rm int}|n'k'\rangle|^2/(\hbar^2\omega^2)\,\delta(E' - E - \hbar\omega - \hbar\omega_q), \qquad (4)$$

where $H_{\rm scat}$ is the Hamiltonian dealing with the scattering mechanisms considered. The scattering matrix element for acoustic deformation scattering is given by

$$\langle n'k'|H_{\rm scat}|nk\rangle = \varepsilon_{\rm ac}[k_B T/2Vc_l]^{1/2}, \qquad (5)$$

where $\varepsilon_{\rm ac}$ is the acoustic deformation potential constant, k_B is Boltzmann's constant, T is the lattice temperature, and c_l is the longitudinal elastic constant. For optical deformation scattering, the matrix element is given by

$$\langle n'k'|H_{\rm scat}|nk\rangle = D\left[\left(N+\frac{1}{2}\mp\frac{1}{2}\right)\hbar/2\rho V\omega_0\right]^{1/2}, \qquad (6)$$

where D is the optical deformation potential constant, ρ is the mass density, and ω_0 is the optical phonon energy.

The various matrix elements will be calculated using the bands determined from the $\boldsymbol{k\cdot p}$ method described above. In the calculations, the energy of the light and heavy hole bands is increased by a constant E_i as the transitions were from an impurity band that was slightly above these bands. This impurity band energy is used as a fitting parameter. The initial carrier motion can be assumed to lie along a chosen direction due to the band isotropy. The excited carrier will still be able to travel in any desired direction.

3. Absorption probability

From the above calculations, the absorption probability is found from

$$\alpha\hbar\omega = \frac{\mu_0 c}{n}2\hbar^2 R/A_0^2 V, \qquad (7)$$

where n is the index of refraction in the material. As this calculation involves only the material parameters and fundamental physical constants, it can be readily adapted by using the appropriate material parameters to different emitter materials in order to tailor the detector response threshold.

B. Carrier scattering rates

The carrier scattering rates for the various scattering processes are needed in order to perform the transport and escape calculations. In the modeling, three basic scattering processes will be considered: (i) ionized impurity scattering, (ii) phonon scattering, and (iii) hot/cold carrier scattering.

The ionized impurity scattering should be significant only in the emitters and was calculated following Ref. 10. This approach includes the effects of screening on the scattering rates. These were calculated once for the emitters with the results being stored for later use in the calculation. The phonon scattering rates were calculated following the approach of Ref. 8. This approach includes the absorption and emission of both optical and acoustic phonons for transitions both within and between the hole bands.

The third scattering process was obtained using an empirical approach. Two scattering lengths were determined, one for the scattering of injected carriers for which the hot carriers are still in the light/heavy hole bands and a second for the photoexcited carriers which would be in the split-off band. The scattering length for the injected carriers in GaAs was determined by fitting the dark current for samples[6] with free carrier thresholds of 4, 6, and 8 μm giving a scattering length of ~80 nm, which is similar to the mean distance between the cold carriers of 75 nm calculated from the doping density in the emitters. The photoexcited carrier scattering length was then obtained by fitting the response of the same samples giving a much longer scattering length of 500 nm. The final carrier direction was chosen randomly in center of mass space. While this approach gave a reasonable explanation of the detector response, it is not clear that it corresponds to the actual physical situation. The assumption of random scattering direction may lead to excess scattering events with high energy transfer between the carriers. In addition, the distance between carriers is much less than that at which a 90° scattering would occur for the hot carriers. This implies that the actual process may involve scattering from multiple centers at once, with much smaller changes in direction from the scattering events. While this effect is typically not observed for cold-cold carrier scattering, it is limited by the fact that most of the possible postscattering states are already occupied, which is not the case for hot-cold carrier scattering. This should be further investigated to develop a full model for the hot-cold carrier scattering.

C. Carrier transport and escape from the emitters

The escape probability determination involves two steps: (i) the actual escape of the carriers at the interface, and (ii) the transport and scattering of the carriers as they move through the emitters to the interface

There are two possible mechanisms for escape of the excited carriers. The first is to directly escape over the barrier while remaining in the same hole band as presently occupied. The probability can be determined using an escape cone model,[11,12] as has been done in previous modeling.[13] This approach simply determines the probability that the energy of the carrier associated with motion perpendicular to the barrier is greater than the barrier height. If needed it could be readily modified to include quantum mechanical tunneling for carriers with energies just below the barrier.

Downloaded 11 Jan 2010 to 131.96.4.68. Redistribution subject to AIP license or copyright; see http://jap.aip.org/jap/copyright.jsp

This approach would include any scattering effects at the interface and results in a change of only a few percent in the escape.

The second mechanism is for the carrier to transfer into a different band as it crosses the emitter/barrier interface. This is possible due to the mixing that occurs between the light, heavy, and split-off hole states. The probability can be calculated from the states on the two sides of the interface using the standard quantum mechanical transmission probability approach. This approach can also be used for more complicated interfaces, such as resonant structures, designed to enhance this transmission probability.

The escape probability for the photoexcited carriers is then obtained by randomly selecting a carrier from the excited carrier distribution and propagating it to the emitter-barrier interface. At the interface, the probability of escape is determined and any unescaping carriers are reflected back into the emitter. The motion of the carrier is followed until it either escapes or has an energy less than the barrier when it is retained in the emitter.

The initial carrier momentum is determined by starting with an unexcited carrier with energy selected randomly from the Fermi distribution. The rates for direct (r_d) and indirect (r_i) transitions at a specific value of k are obtained as described above. The carrier excitation process was then determined with probability $r_d/(r_d+r_i)$ for a direct and $r_i/(r_i+r_d)$ for an indirect process. If a direct excitation occurs, the final momentum is then determined from the excited energy by $p=\sqrt{2m^*E}$ with a random initial direction. For an indirect excitation, the carrier was assumed to be traveling in a random direction before excitation, and the phonon was selected randomly from the phonon distribution. Momentum conservation was then used to determine the final carrier momentum. The excited carriers were assumed to travel in a straight line until scattering or reaching the interface. For scattering, the scattering process is determined using the scattering rates calculated above, and a new carrier energy and momentum are calculated and the process is repeated. At the interface, the carrier either escapes or is reflected based on the probabilities calculated as in Sec. II B.

D. Trapping of injected carriers

The trapping probability for the carriers injected from the contact was performed following the same procedure. This is essentially the same procedure followed in previous modeling[13] to calculate the escape and trapping except that here the concentration is on the processes involving the split-off band and that the transmission at the interface is calculated quantum mechanically using the wave functions as well as using an escape cone.

E. Dark and illuminated current calculations

The calculation of dark and illuminated currents then followed the same basic procedure. This will be described first for the dark current. In the preliminary calculations, the detector was assumed to consist of only a single emitter to simplify the calculations. However, the same process can be applied to detectors with multiple emitters.

First, the injection current density and the escape current from the emitter were calculated using

$$j_{(inj)}(E_x) = qn_c(E_x)T(E_x,F_e), \tag{8}$$

where q is the electron charge, n_c is the number of electrons per unit area per unit energy per unit time incident on the barrier with energy E_x, and $T(E_x,F_e)$ is the transmission probability for the incident electrons with energy E_x and electric field F_e. The transmission probability was calculated following Gundlach.[14] The incident hole distribution is simply the standard Fermi distribution integrated over the directions parallel to the plane of the well giving $n_c=(4\pi mkT/h^3)\ln(1+e^{E_x/kT})$. The injected carriers were propagated through the structure following the same procedure used for the photoexcited carriers and the trapping probability P_t in the emitter determined. The dark current was then found determined by requiring that the trapping and thermal escape in the emitters was balanced giving

$$n_e = n_t, \tag{9}$$

where n_e and n_t are the numbers of carriers escaping from and being trapped in the emitter per unit time. Based on the experimental results, for this condition to occur it was found that the field at the injection contact should be much lower than the mean field in the detector to match the experimentally measured dark currents. This leads to the field being low across all but the final barrier layer with space charge building up in the final emitter layer. Both the dark and photocurrents were limited by this last emitter, and hence in all further calculations only this emitter was considered.

Next the emitter was assumed to be illuminated and the photoexcitation rate determined by multiplying the absorption probability by the incident photon density was included in the escape mechanisms for the emitter,

$$n_e + n_p = n_t, \tag{10}$$

where n_p is the number of escaping photoexcited carriers per unit time. This change in the escape rate is the only difference in the calculations and the illuminated current was determined from requiring the escape and trapping rates to be the same. The photocurrent was then determined by subtracting the dark current from the illuminated current.

$$j_{\text{ph}} = j_{\text{illum}} - j_{\text{dark}}. \tag{11}$$

III. COMPARISON WITH EXPERIMENTS

This model was tested by comparing the calculated results with experimental measurements for three samples having free-carrier thresholds wavelength of 4, 6, and 8 μm. The results gave reasonable agreement with the predicted peak response being within ~20% of the measured value for all the biases, as seen in Fig. 1, for the sample with a 4 μm threshold. The results for the 6 and 8 μm threshold samples were similar. The increases in response due to the split-off transitions can be clearly seen in the response. For the short wavelength end, the slope of the response did not vary with bias when all the curves were normalized to the same peak value at 2.9 μm. This slope also was not sensitive to the

Downloaded 11 Jan 2010 to 131.96.4.68. Redistribution subject to AIP license or copyright; see http://jap.aip.org/jap/copyright.jsp

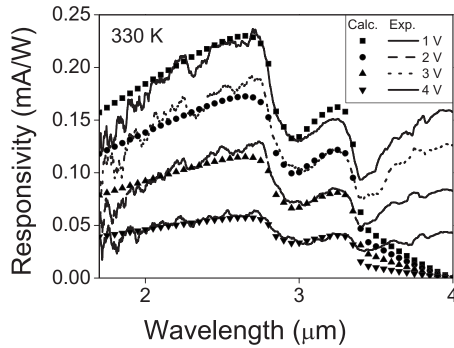

FIG. 1. The experimental spectra and the calculated response using the model for a sample having a 4 μm free-carrier threshold. There is good agreement except at the longer wavelengths. The disagreement at long wavelengths is due to the thermal mechanism which is not included in the model.

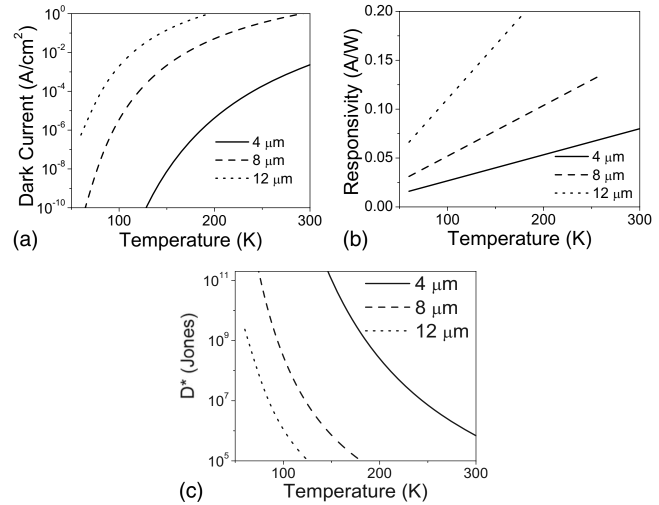

FIG. 2. (a) The dark current, (b) responsivity, and (c) detectivity for detectors with free-carrier thresholds of 4, 8, and 12 μm at different temperatures at a bias of 1.0 V. The fixed detector parameters were w_e=20 nm, $n_e=3\times10^{18}$ cm^{-3} w_t=50 nm, and w_b=1000 nm. By varying the free-carrier threshold, it is possible to select the optimum combination of responsivity, D^*, and operating temperature for a specific application.

scattering length. The deviation seen at long wavelengths beyond ~3.5 μm appears to be due to a thermal detection mode that is also present, which is not included in the modeling. Inclusion of this mechanism would improve the fit at wavelengths longer than the free-carrier threshold. All these samples had capture probabilities ~1 for the hot carriers and hence, the device should have a photoconductive gain of 1 with only the last emitter contributing to the photoresponse. The model gives a photocurrent gain of 0.95 ± 0.05 which is in agreement with the predicted value of 1.0 for a single emitter detector with all the injected current being trapped in the emitter. The experimentally obtained noise current gain is ~0.2 for a detector with 30 emitters. Unlike in quantum well infrared photodetectors (QWIPs), the noise gain in split-off detectors is less than the photocurrent gain. In QWIPs, the noise is introduced at the injection contact and then experiences the same gain as the photocurrent. Thus for a QWIP, the total noise or photocurrent gain $g=g_1/N$,[15] where g_1 is the single layer gain and N is the number of layers. However, for the split-off detectors that were measured, the emitters and the contact have identical parameters and at each successive emitter all the carriers will be captured. Thus each emitter will introduce its own noise factor which will add incoherently with the other emitters. This increases the noise by a factor of $N^{1/2}$, giving a noise gain of $g_1/N^{1/2}$. Using the single emitter gain as 1, for a detector with 30 emitters, this would give a value of 0.18, which is in reasonable agreement with the ~0.2 obtained experimentally.

IV. EFFECTS OF PARAMETER VARIATION

Using the carrier-carrier scattering lengths obtained from the fitting above, the effects of varying design parameters were investigated. For the calculations, the device structure consisted from bottom to top of a GaAs bottom contact of thickness w_c with p-doping n_c, an undoped AlGaAs barrier layer of thickness[1] w_b and Al fraction x_b, a p-doped GaAs emitter of thickness w_e and doping n_e, a top AlGaAs barrier with thickness w_t and Al fractions x_{t1} and x_{t2} at the bottom of the barrier, respectively, and a GaAs top contact of thickness w_c with p-doping n_c. By using different values for x_{t1} and x_{t2}, it is possible to include a graded barrier in the designs. For all calculations, the contact parameters were w_c=0.1 μm and $n_c=1\times10^{19}$ cm^{-3}.

The first parameter tested was the barrier height. For the calculations, the emitter parameters were fixed at w_e =20 nm and $n_e=3\times10^{18}$ cm^{-3} to match the devices tested. The top and bottom barrier thicknesses were 50 and 1000 nm, respectively. The three Al fractions were set to the same value, which was adjusted to vary the free-carrier threshold. A plot of the dark current density for three detectors with free-carrier thresholds of 4, 6, and 8 μm is given in Fig. 2(a) showing a rapid decrease in the dark current with temperature. The variations in dark current density, response, and detectivity at 1.0 V with temperature and free-carrier threshold are shown in Fig. 2. As can be seen, the response is higher for longer free-carrier thresholds, while the dark current is lower for shorter free-carrier thresholds. This property will allow the detectors to be designed with the optimum combination of response and operating temperature for specific applications.

The effects of varying the emitter thickness on the response and the detectivity with $n_e=3\times10^{18}$ cm^{-3} for detectors with 4, 6, and 8 μm free-carrier thresholds are shown in Fig. 3. The response increased as the emitter thickness increased up to a value of ~50 nm due to the increasing absorption. For thicker emitters, the escape probability started to decrease, leading to a reduced response for emitters thicker than 50 nm. The dark current did not vary with emitter thickness as the injected carriers were already trapped nearly 100% of the time for the thinnest emitter studied. The effects of increasing the emitter doping are shown in Fig. 4 with increased response at higher doping due to the increased absorption. This would indicate that optimum response will be obtained at higher doping levels. However, these curves should be treated with some caution as the hot-cold carrier scattering lengths were not adjusted for doping effects as

Downloaded 11 Jan 2010 to 131.96.4.68. Redistribution subject to AIP license or copyright; see http://jap.aip.org/jap/copyright.jsp

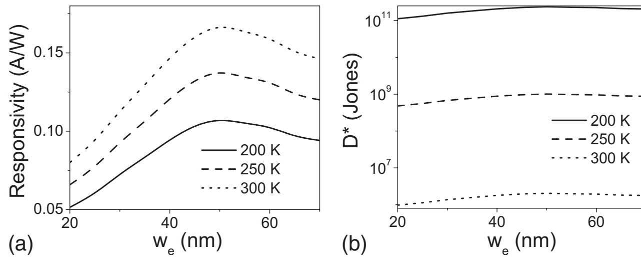

FIG. 3. (a) The responsivity and (b) detectivity variation with emitter width for a detector with a free-carrier threshold of 4 μm at three different temperatures at a bias of 1.0 V. The fixed detector parameters were $n_e=3\times 10^{18}$ cm^{-3}, $w_t=50$ nm, and $w_b=1000$ nm. The response increases up to 50 nm and then starts to decrease.

they are empirically determined numbers. Increased scattering at high doping could reduce the response, and further work on the effects of doping on the scattering are needed before a final conclusion on optimum emitter doping levels and thicknesses can be reached.

The results above showed two important properties for the carrier transport in the devices. The first is that as all the carriers were trapped at the emitter, adding additional emitters would not lead to increased response. While adding additional emitters would increase the absorption, it also decreases the gain by the same factor leading to no net improvement in the response. The second is that the trapping of the carriers in the emitters lead to a significant space charge buildup in the emitters if the emitter and contact doping were not the same. In order to reduce the trapping and hence increase the gain, grading the top barrier in order to produce an offset between the barriers on the two sides of the emitter was explored. Using this approach it might also be possible to use multiple emitters under conditions where the gain could be kept near 1, allowing increased absorption. When the barrier on the injection side of the emitter is higher than that on the escape side, it will artificially heat the carriers entering the emitter. If the difference in heights is sufficiently large, the carriers will still be able to escape after scattering and the trapping rate will be greatly reduced. Grading the Al fraction in the top will allow the thermal escape from the contact and the emitter to be balanced reducing space charge buildup, which reduces the responsivity. The increase in response with the difference in barrier height is shown in Fig. 5. In designing detectors, the fact that the gain applies to both the dark and photocurrents will need to be considered to determine the optimum value. The results indicate that increasing the gain above ~3 will not lead to any increase in D^* even though the response increases.

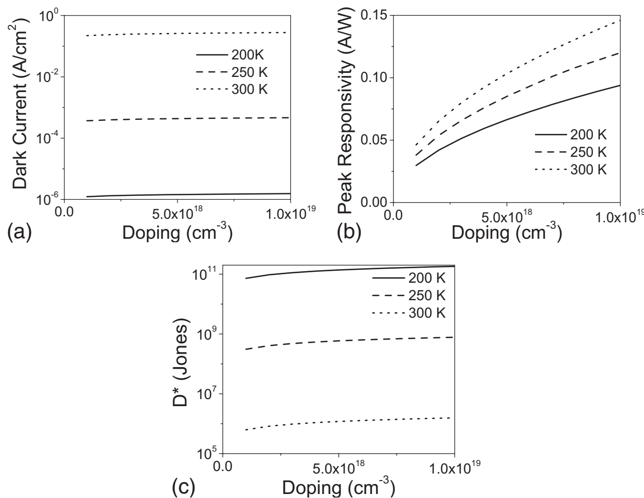

FIG. 4. (a) The dark current, (b) responsivity, and (c) detectivity variation with emitter doping for a detector with a free-carrier threshold of 4 μm at three different temperatures at a bias of 1.0 V. The fixed detector parameters were $w_e=20$ nm, $w_t=50$ nm, and $w_b=1000$ nm. Increasing doping lead to increased absorption and hence increased response, while the dark current was only slightly increased.

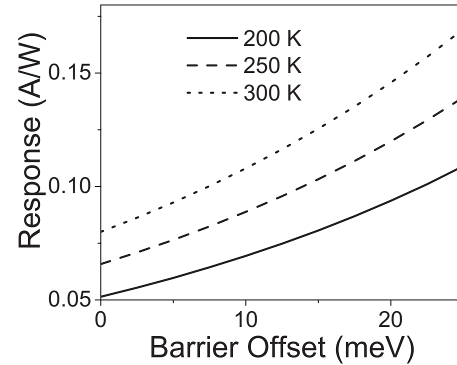

FIG. 5. The responsivity variation with barrier offset for a detector with a free-carrier threshold of 4 μm at three different temperatures at a bias of 1.0 V. The fixed detector parameters were $w_e=20$ nm, $n_e=3\times 10^{18}$ cm^{-3} $w_t=50$ nm, and $w_b=1000$ nm. The Al fraction in the top barrier was graded so that the injection from the contact and emitter were the same.

Another potential improvement is the use of a double barrier structure to increase escape of holes from the split-off to the light/heavy hole bands by bringing the two bands into resonance. By using a resonant state in the double barrier, which can be coupled to the states in the emitter, it should be possible to enhance the escape from the split-off band into the light hole band. While this might also be achieved without using a double barrier structure, the ability to fine-tune the resonance using bias will make the double barrier approach less sensitive to variations in Al fraction. The results for including a resonant structure on the detector are shown in Fig. 6. Here the inclusion of the resonant structure has increased the response by a factor of ~85. Because the spectral shape is determined by the transitions from the light/heavy to split-off hole bands, this increased response is observed at all wavelengths.

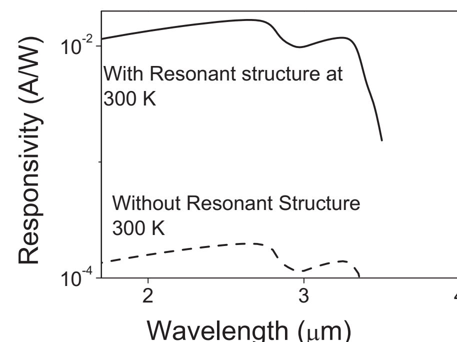

FIG. 6. The increased response from the inclusion of a resonant structure to enhance coupling of the split-off band in the emitter to the light/heavy hole bands in the barrier. The response has been increased by a factor of ~85.

Downloaded 11 Jan 2010 to 131.96.4.68. Redistribution subject to AIP license or copyright; see http://jap.aip.org/jap/copyright.jsp

V. CONCLUSIONS

A model has been presented for the response in split-off band detectors. It included the photoabsorption from the split-off band transitions, escape by scattering to the light/heavy hole band or by direct quantum mixing of the states. The model was used to explain the response of an experimentally measured detector. Based on the modes, an optimized detector was suggested.

ACKNOWLEDGMENTS

This work was supported by the U.S. Army under Grant No. W911NF-08-1-0448.

[1]N. T. Gordon, D. J. Rees, G. Bowen, T. S. Phillips, M. Haigh, C. L. Jones, C. D. Maxey, L. Hipwood, and R. A. Catchpole, J. Electron. Mater. **35**, 1140 (2006).
[2]H. Alause, W. Knap, J. L. Robert, R. Planel, V. Thierry-Mieg, F. H. Julien, K. Zekentes, and V. Mossed, Semicond. Sci. Technol. **15**, 724 (2000).
[3]G. Ariyawansa, A. G. U. Perera, X. H. Su, S. Chakrabarti, and P. Battacharya, Infrared Phys. Technol. **50**, 156 (2007).
[4]E. Plis, J. B. Rodriguez, H. S. Kim, G. Bishop, Y. D. Sharma, L. R. Dawson, S. Krishnaa, S. J. Lee, C. E. Jones, and V. Gopal, Appl. Phys. Lett. **91**, 133512 (2007).
[5]A. G. U. Perera, S. G. Matsik, P. V. V. Jayaweera, K. Tennakone, H. C. Liu M. Buchanan G. Von Winckel, A. Stintz, and S. Krishna, Appl. Phys. Lett. **89**, 131118 (2006).
[6]P. V. V. Jayaweera, S. G. Matsik, A. G. U. Perera, H. C. Liu, M. Buchanan, and Z. R. Wasilewski, Appl. Phys. Lett. **93**, 021105 (2008).
[7]E. O. Kane, in *Semiconductors and Semimetals*, edited by R. K. Willardson and A. C. Beer (Academic, New York, 1966), Vol. 2, p . 75.
[8]R. Scholz, J. Appl. Phys. **77**, 3219 (1995).
[9]K. Seeger, *Semiconductor Physics*, 5th ed. (Springer-Verlag, Berlin, 1991), Chap. 6.
[10]T. Brudevoll, T. A. Fjeldly, J. Baek, and M. S. Shur, J. Appl. Phys. **67**, 7373 (1990).
[11]V. E. Vickers, Appl. Opt. **10**, 2190 (1971).
[12]J. M. Mooney and J. Silverman, IEEE Trans. Electron Devices **32**, 33 (1985).
[13]S. G. Matsik and A. G. U. Perera, J. Appl. Phys. **104**, 044502 (2008).
[14]K. H. Gundlach, Solid-State Electron. **9**, 949 (1966).
[15]H. C. Liu, Appl. Phys. Lett. **61**, 2703 (1992).

Downloaded 11 Jan 2010 to 131.96.4.68. Redistribution subject to AIP license or copyright; see http://jap.aip.org/jap/copyright.jsp